

FROM PLANETESIMAL TO PLANET IN TURBULENT DISKS. II. FORMATION OF GAS GIANT PLANETS

HIROSHI KOBAYASHI

Department of Physics, Nagoya University, Nagoya, Aichi 464-8602, Japan

HIDEKAZU TANAKA

Astronomical Institute, Tohoku University, Aramaki, Aoba-ku, Sendai 980-8578, Japan

Draft version June 20, 2018

ABSTRACT

In the core accretion scenario, gas giant planets are formed from solid cores with several Earth masses via gas accretion. We investigate the formation of such cores via collisional growth from kilometer-sized planetesimals in turbulent disks. The stirring by forming cores induces collisional fragmentation and surrounding planetesimals are ground down until radial drift. The core growth is therefore stalled by the depletion of surrounding planetesimals due to collisional fragmentation and radial drift. The collisional strength of planetesimals determines the planetesimal-depletion timescale, which is prolonged for large planetesimals. The size of planetesimals around growing cores is determined by the planetesimal size distribution at the onset of runaway growth. Strong turbulence delays the onset of runaway growth, resulting in large planetesimals. Therefore, the core mass evolution depends on turbulent parameter α ; the formation of cores massive enough without significant depletion of surrounding planetesimals needs strong turbulence of $\alpha \gtrsim 10^{-3}$. However, the strong turbulence with $\alpha \gtrsim 10^{-3}$ leads to a significant delay of the onset of runaway growth and prevents the formation of massive cores within the disk lifetime. The formation of cores massive enough within several millions years therefore requires the several times enhancement of the solid surface densities, which is achieved in the inner disk $\lesssim 10$ AU due to pile-up of drifting dust aggregates. In addition, the collisional strength Q_D^* even for kilometer-sized or smaller bodies affects the growth of cores; $Q_D^* \gtrsim 10^7$ erg/g for bodies $\lesssim 1$ km is likely for this gas giant formation.

Subject headings: planets and satellites: formation — planets and satellites: gaseous planets

1. INTRODUCTION

Gas giant planets such as Jupiter, Saturn, and massive exoplanets are formed in protoplanetary disks containing solid and gas. In the core accretion scenario, once planetary embryos grow to $\sim 5M_\oplus$, planetary atmospheres that Mars sized or larger embryos acquire become too massive to keep hydrostatic states, resulting in the rapid gas accretion to form gas giants (e.g., Mizuno 1980). Therefore, gas giant formation requires such massive solid cores to be formed within the disk lifetime (~ 4 Myr).

In protoplanetary disks, sub-micron sized dust grains accumulate to be planetesimals. Collisional growth of grains produces centimeter sized or larger particles, which drift onto the host star on significantly short timescales due to moderate coupling with gas. If particles accumulate up to the Roche density, gravitational instability creates kilometer sized or larger planetesimals (Goldreich & Ward 1973; Youdin & Goodman 2005; Michikoshi et al. 2012; Takeuchi & Ida 2012). On the other hand, collisional growth of dust grains naturally form fluffy aggregates (Suyama et al. 2008, 2012). The bulk density of dust aggregates becomes $\sim 10^{-4}$ g/cm³ and the collisional growth timescale of such bodies is much shorter than their drift timescale, so that kilometer sized planetesimals are formed via direct collisional growth prior to radial drift (Okuzumi et al. 2012).

Planetesimals grow through mutual collisions. In a turbulent disk, the stirring by turbulence increases the random velocity of planetesimals v_r . For large v_r , the gravitational focusing of planetesimals is negligible and the orderly growth occurs until $v_r \gtrsim 1.5v_{\text{esc}}$ (Kobayashi et al. 2016), where v_{esc} are the surface escape velocities of planetesimals. In the orderly growth, the mass-weighted average radius of planetesimals is comparable to the radius of largest planetesimals. As planetesimals grow, v_{esc} increases to $\sim v_r$, runaway growth occurs (Wetherill and Stewart 1989). The mass-weighted average radius of planetesimals at the onset of runaway growth, which is determined by turbulent strength (Kobayashi et al. 2016), almost remains the same after runaway growth.

Runaway growth forms a planetary embryo in each annulus of the disk. Embryos further grow mainly through collisions with surrounding planetesimals. As embryos become massive, their viscous stirring increases v_r , resulting in destructive collisions between planetesimals. Collisional fragments of planetesimals get further smaller via collisions between themselves. This collisional cascade decreases the size of bodies until radial drift. This process reduces surrounding planetesimals and embryo growth is then stalled (Kobayashi et al. 2010).

Collisional strength depends on the radius of planetesimals, r (e.g., Benz & Asphaug 1999). For $r \gtrsim 1$ km, the collisional outcome of a single collision is controlled by the self-gravity of colliders so that larger bodies are effectively stronger for collisions. Larger

planetesimals, which have a longer collisional depletion timescales, contribute more to the growth of massive embryos. Embryo growth strongly depends on the mass-weighted average radius of planetesimals surrounding embryos (Kobayashi et al. 2010, 2011; Kobayashi & Dauphas 2013), which is mainly determined by the strength of turbulence (Kobayashi et al. 2016). Therefore, the growth and formation of solid cores of gas giants depends on the strength of disk turbulence.

In this paper, we investigate gas giant planet formation via core accretion in turbulent disks. In § 2, we introduce the critical core mass from simple analysis. In § 3, we explain the model of simulations. In § 4, we perform simulations of collisional evolution of bodies from $r = 1$ km. We show the dependence of embryo growth on turbulent strength and collisional property and find the conditions for the formation of cores massive enough for the onset of rapid gas accretion to form gas giants. In § 5, we discuss the growth timescale of embryos in turbulent disks, and the type I migration of growing embryos and the gas dispersal timescale of disks. In § 6, we summarize our findings.

2. CRITICAL CORE MASS

The runaway growth of planetesimals produces a planetary embryo with mass M_E and radius R_E in each annulus of a protoplanetary disk. Once R_E is larger than its Bondi radius, R_B defined by $R_B = GM_E/c_s^2$, the embryo has an atmosphere, where G is the gravitational constant and c_s is the sound velocity of gas. The density of a hydrostatic atmosphere, ρ_a , at the distance R from the center of the planetary embryo is given by (derivation in Appendix A; Mizuno 1980; Stevenson 1982; Inaba & Ikoma 2003)

$$\rho_a = \frac{\pi\sigma_{\text{SB}}}{12\kappa L_e R^3} \left(\frac{GM_E \mu m_H}{k} \right)^4, \quad (1)$$

where σ_{SB} is the Stefan-Boltzmann constant, κ is the opacity of the atmosphere, k is the Boltzmann constant, μ is the mean molecular weight, m_H is the mass of a hydrogen atom, and L_e is the planetary luminosity. The accretion of bodies onto planetary embryos mainly determines L_e so that

$$L_e = \frac{GM_E}{R_E} \frac{dM_E}{dt}. \quad (2)$$

The total atmospheric mass, M_A , is given by

$$M_A = \int_{R_E}^{R_B} 4\pi R^2 \rho_a dR, \quad (3)$$

$$= \frac{\pi^2 \sigma_{\text{SB}} G^3 M_E^3 R_E}{3\kappa M_E} \left(\frac{\mu m_H}{k} \right)^4 \ln \left(\frac{R_B}{R_E} \right). \quad (4)$$

Once M_A is comparable to M_E , the hydrostatic atmosphere is not maintained and then rapid gas accretion occurs to form gas giants. The embryo mass at the onset of rapid gas accretion is called the critical core mass, which is approximately estimated from $M_A/M_E \approx 1/3$ (Mizuno 1980; Stevenson 1982; Ikoma et al. 2000). Using Eq. (4) with $M_A = M_E/3$, the critical core mass M_{crit} is given by

$$M_{\text{crit}} = 5M_{\oplus} \left(\frac{M_E/\dot{M}_E}{10 \text{ Myr}} \right)^{-3/4} \left(\frac{\kappa}{0.01 \text{ cm}^2 \text{ g}^{-1}} \right)^{3/4}, \quad (5)$$

where the dependence of $\ln(R_B/R_E)$ on M_E is ignored for this derivation.

Therefore, forming embryos with $M_E \gtrsim 5M_{\oplus}$ are required for giant planet formation via core accretion. Note that the critical core mass may be smaller than $5M_{\oplus}$ because the depletion of planetesimals due to collisional fragmentation results in smaller \dot{M}_E (e.g., Kobayashi et al. 2011).

We below perform simulations for the formation and growth of embryos and find conditions for the formation of embryos with the critical core mass. Although we here simply estimate M_A using the radiative temperature gradient with constant κ , we calculate M_A from M_E and \dot{M}_E obtained in simulations, taking into account the convective temperature gradient as well as the radiative one with κ dependent on temperature (Inaba & Ikoma 2003).

3. MODEL FOR PLANETARY ACCRETION

The surface number density of planetesimals with masses m to $m + dm$ orbiting around the host star with mass M_* at the distance a , $n_s(m, a)dm$, evolves through collisions and radial drift. The governing equation is given as (e.g., Kobayashi et al. 2016),

$$\begin{aligned} \frac{\partial m n_s(m, a)}{\partial t} = & \frac{m}{2} \int_0^\infty dm_1 \int_0^\infty dm_2 n_s(m_1, a) n_s(m_2, a) \\ & \times K(m_1, m_2) \delta(m - m_1 - m_2 + m_e) \\ & - m n_s(m) \int_0^\infty dm_2 n_s(m_2, a) K(m, m_2) \\ & + \frac{\partial}{\partial m} \int_0^\infty dm_1 \int_0^{m_1} dm_2 n_s(m_1, a) n_s(m_2, a) \\ & \times K(m_1, m_2) \Psi(m, m_1, m_2) \\ & - \frac{1}{a} \frac{\partial}{\partial a} [a m n_s(m, a) v_{\text{drift}}(m, a)], \end{aligned} \quad (6)$$

where the collisional kernel $K(m_1, m_2)$ between bodies with masses m_1 and m_2 is given by

$$K(m_1, m_2) = (h_{m_1, m_2} a)^2 \langle \mathcal{P}_{\text{col}}(m_1, m_2) \rangle \Omega, \quad (7)$$

with the reduced mutual Hill radius $h_{m_1, m_2} = [(m_1 + m_2)/3M_*]^{1/3}$, the dimensionless mean collisional rate $\langle \mathcal{P}_{\text{col}}(m_1, m_2) \rangle$, and the Kepler orbital frequency Ω , m_e and $\Psi(m, m_1, m_2)$ are, respectively, the total and cumulative masses of bodies produced by a single collision between bodies with masses m_1 and m_2 , and v_{drift} is the drift velocity of a body due to gas drag. The collisional rate is determined according to the orbits of colliding bodies and the amount of their atmospheres: $\langle \mathcal{P}_{\text{col}}(m_1, m_2) \rangle$ is given by a function of relative eccentricities and inclinations between bodies and the accretion rates of the bodies, which are summarized in Inaba et al. (2001). The enhancement of collisional cross-section due to embryo's atmosphere (Inaba & Ikoma 2003) and due to gas drag for small bodies (Ormel & Klahr 2010) is taken into account. The atmospheric opacity is given by the sum of those of gas and grains, given by

(Inaba & Ikoma 2003)

$$\kappa = \begin{cases} 0.01 + 4f \text{ cm}^2 \text{ g}^{-1} & \text{for } T \leq 170 \text{ K}, \\ 0.01 + 2f \text{ cm}^2 \text{ g}^{-1} & \text{for } 170 \text{ K} < T \leq 1700 \text{ K}, \\ 0.01 \text{ cm}^2 \text{ g}^{-1} & \text{for } T > 1700 \text{ K}, \end{cases} \quad (8)$$

where f is the grain depletion factor comparing to the interstellar one. The effective growth of dust aggregates deplete the opacity significantly (Okuzumi et al. 2012), so that we put $f = 10^{-4}$.

The collisional kernel depends on orbital eccentricities e and inclinations i of colliders, which depend on mass m and distance a . The time variation of $e(m, a)$ and $i(m, a)$ via gravitational interactions between bodies depends on the mass distribution of bodies. Therefore, the evolution of $e(m, a)$ and $i(m, a)$ have to be treated simultaneously with collisional evolution. The square of dispersions for eccentricities and inclinations of bodies evolve according to

$$\frac{de^2(m, a)}{dt} = \left. \frac{de^2}{dt} \right|_g + \left. \frac{de^2}{dt} \right|_d + \left. \frac{de^2}{dt} \right|_c + \left. \frac{de^2}{dt} \right|_t, \quad (9)$$

$$\frac{di^2(m, a)}{dt} = \left. \frac{di^2}{dt} \right|_g + \left. \frac{di^2}{dt} \right|_d + \left. \frac{di^2}{dt} \right|_c + \left. \frac{di^2}{dt} \right|_t, \quad (10)$$

where the subscripts “g”, “d”, “c”, and “t” indicate gravitational interaction between bodies (Ohtsuki et al. 2002), damping by gas drag (Adachi et al. 1976), collisional damping (Ohtsuki 1992), and turbulent stirring due to density fluctuation (Okuzumi & Ormel 2013) and aerodynamical friction (Völk et al. 1980), respectively. We use the damping rates by gas drag linear functions of e and i given by Inaba et al. (2001) because e and $i \ll 1$, although the e and i damping rates by gas drag are greater for higher e and i (Kobayashi 2015). We use the damping rate and radial drift due to gas drag, taking into account three gas drag regimes (see details in Kobayashi et al. 2010).

For 10 meter-sized or larger bodies, the stirring by turbulence is mainly caused by turbulent density fluctuation, given by (Okuzumi & Ormel 2013)

$$\left. \frac{de^2}{dt} \right|_t \approx f_d \left(\frac{\Sigma_g a^2}{M_*} \right)^2 \Omega, \quad (11)$$

$$\left. \frac{di^2}{dt} \right|_t \approx \epsilon^2 \left. \frac{de^2}{dt} \right|_t, \quad (12)$$

where Σ_g is the gas surface density, f_d is the dimensionless factor, and $\epsilon = 0.01$ (see Kobayashi et al. 2016). According to the magnetohydrodynamical simulations, f_d is given by (Okuzumi & Ormel 2013),

$$f_d = \frac{0.94\alpha}{(1 + 4.5H_{\text{res},0}/H)^2}, \quad (13)$$

where H is the scale height of the disk, $H_{\text{res},0}$ is the half vertical width of the dead zone, α is the dimensionless turbulent viscosity at the midplane. For simplicity, we set $H_{\text{res},0} = H$.

Dynamical stirring by large bodies increases collisional velocities of bodies. The collisional outcome is determined by m_e and $\Psi(m, m_1, m_2)$ in Eq. (6), which are mainly controlled by the fragmentation energy Q_D^* (see

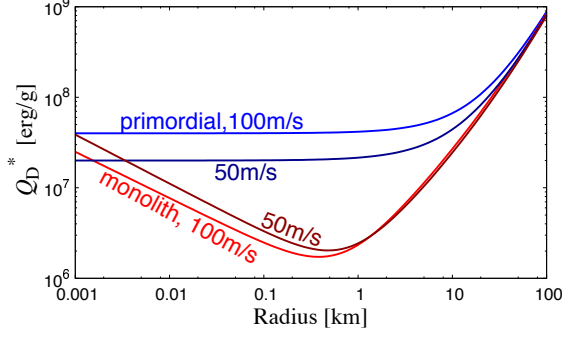


FIG. 1.— The fragmentation energy Q_D^* for primordial and monolith bodies with impact velocities of 50 m/s and 100 m/s, given in Eqs. (14)–(19).

detailed setting Appendix B). We use the following formula for Q_D^* ;

$$Q_D^* = Q_{0s} \left(\frac{r}{1 \text{ cm}} \right)^{\beta_s} + Q_{0g} \rho_s \left(\frac{r}{1 \text{ cm}} \right)^{\beta_g} + C_{\text{gg}} \frac{2Gm}{r}, \quad (14)$$

where ρ_s is the density of a body, Q_{0s} , Q_{0g} , β_s , β_g , and C_{gg} characterize the collisional strength. On the right hand side of Eq. (14), the first term is dominant for kilometer sized or smaller bodies. The second term is important for larger bodies. The third term is determined by pure gravity, which is dominant for $r \gtrsim 10^7 \text{ cm}$: we set $C_{\text{gg}} = 10$ (Stewart & Leinhardt 2009). The values of Q_{0s} , Q_{0g} , β_s , and β_g depend on the impact velocity (e.g., Benz & Asphaug 1999) and the structure of a body (e.g., Wada et al. 2013). For monolith bodies, these values are estimated from the interpolation of simulation data for the impact velocities v_{imp} of 3 and 5 km/s obtained by Benz & Asphaug (1999), given by

$$Q_{0s} = 1.6 \times 10^7 \left(\frac{v_{\text{imp}}}{3 \text{ km/s}} \right)^{\gamma_{\text{sv}}} \text{ erg/g}, \quad (15)$$

$$\beta_s = -0.39 \left(\frac{v_{\text{imp}}}{3 \text{ km/s}} \right)^{\gamma_{\text{bsv}}}, \quad (16)$$

$$Q_{0g} = 1.2 \left(\frac{v_{\text{imp}}}{3 \text{ km/s}} \right)^{\gamma_{\text{gv}}} \text{ erg cm}^3/\text{g}^2, \quad (17)$$

$$\beta_g = 1.26 \left(\frac{v_{\text{imp}}}{3 \text{ km/s}} \right)^{\gamma_{\text{bgv}}}, \quad (18)$$

where $\gamma_{\text{sv}} = -0.82$, $\gamma_{\text{gv}} = -0.31$, $\gamma_{\text{bsv}} = -0.080$, and $\gamma_{\text{bgv}} = 0.032$. However, growing bodies via collisions are porous (e.g., Wada et al. 2013), which might not have monolith-like structures until melting. Therefore, bodies smaller than about 10 km have Q_D^* of porous bodies, which is given by (Wada et al. 2013),

$$Q_{s0} = 4 \times 10^7 \left(\frac{v_{\text{imp}}}{100 \text{ m/s}} \right) \text{ erg/g}, \quad (19)$$

$$\beta_s = 0. \quad (20)$$

We investigate the growth of melted bodies (monolith) and primordial bodies. For melted bodies, Q_D^* is given by Eqs. (15)–(18). For primordial bodies, Q_D^* is calculated from Eqs. (17)–(20). For melted and primordial bodies, Q_D^* are shown in Fig. 1.

4. MASS EVOLUTION OF BODIES

We perform simulations for planet formation in disks from 4.8 to 26 AU via the time integration of Eqs. (6), (9), and (10) for $M_* = M_\odot$, where M_\odot is the solar mass. The disk is divided into 10 annuli and the mass distribution is described using mass bins with radii between adjacent mass bins 1.05. We fix the bulk density of bodies at $\rho_s = 1 \text{ g/cm}^3$; the mass-radius relation is given by $m = 4\pi\rho_s r^3/3$. The mass corresponding to the smallest mass bin is set to $4.2 \times 10^6 \text{ g}$ ($r = 1 \text{ m}$). We set the initial bodies at radius of 1 km. The bodies initially have $e = i/\sqrt{\epsilon} = 3v_{\text{esc}}/a\Omega \approx 9.9 \times 10^{-5}$. The collisional growth of bodies is almost independent of the initial radius and orbits of bodies if the new born planetesimals are smaller than those at the onset of runaway growth (Kobayashi et al. 2016).

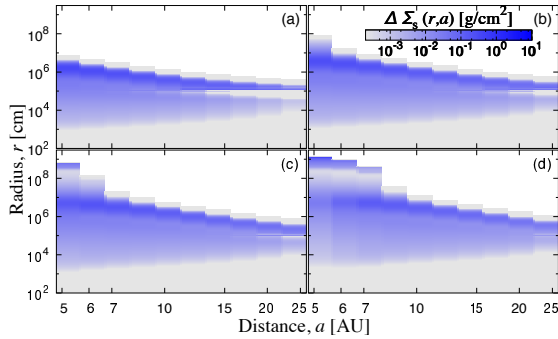


FIG. 2.— Size distribution for mass surface density $\Delta\Sigma_s(r, a)$ of bodies at $2.2 \times 10^5 \text{ yr}$ (a), $7.2 \times 10^5 \text{ yr}$ (b), $1.4 \times 10^6 \text{ yr}$ (c), and $3.3 \times 10^6 \text{ yr}$ (d) in a disk with $x_s = x_g = 3$ for $\alpha = 3 \times 10^{-3}$ with collisional fragmentation for primordial collisional strength, as a function of the distance from the host star, a , and the radius of bodies corresponding to their mass m .

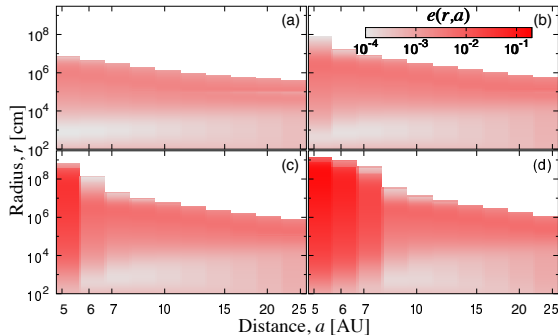


FIG. 3.— Orbital eccentricity distribution obtained from the same simulation as Fig. 2.

The initial surface densities of solid and gas, $\Sigma_{s,0}$ and $\Sigma_{g,0}$, are, respectively, set to have power-law radial distributions;

$$\Sigma_{g,0} = 1700 x_g \left(\frac{a}{1 \text{ AU}} \right)^{-1.5} \text{ g cm}^{-2}, \quad (21)$$

$$\Sigma_{s,0} = 30 x_s \left(\frac{a}{1 \text{ AU}} \right)^{-1.5} \text{ g cm}^{-2}, \quad (22)$$

where x_g and x_s are the scaling factors and the disk with $x_g = x_s = 1$ corresponds to the minimum-mass solar

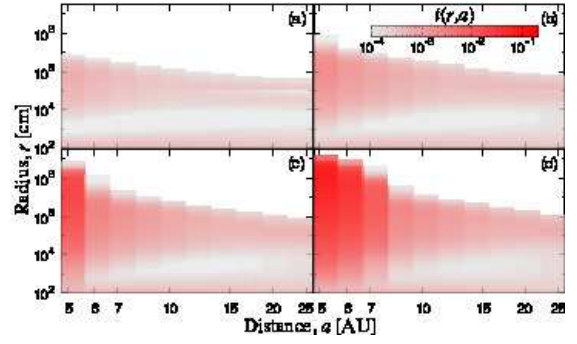


FIG. 4.— Orbital inclination distribution obtained from the same simulation as Fig. 2.

nebula (MMSN) model (Hayashi 1981). The solid surface density Σ_s evolves due to the radial drift of bodies, while the gas surface density artificially decreases from the formula $\Sigma_g = \Sigma_{g,0} \exp(-t/\tau_{\text{gas}})$ with $\tau_{\text{gas}} = 10^7 \text{ yr}$. We discuss τ_{gas} and the time dependence of depletion in § 5. In addition, we set the temperature at the disk midplane as

$$T = 280 \left(\frac{a}{1 \text{ AU}} \right) \text{ K}, \quad (23)$$

which affects R_B and the aerodynamical turbulent stirring. However, they are unimportant for the evolution of M_E and M_A .

We show the size and velocity evolution of bodies in the whole disk in § 4.1 and focus on the size and velocity distributions around 5 AU in § 4.2. The evolution of planetary embryos dependent on α is shown in § 4.3. We discuss the formation of cores with the critical core masses from M_E and M_A obtained within disk lifetimes by simulations in § 4.4.

4.1. Size and Velocity Evolution of Bodies in the Whole Disk

We perform a simulation for planet formation with primordial strength in the disk with $x_s = x_g = 3$ (3MMSN) for $\alpha = 3 \times 10^{-3}$, which results in the size and orbit evolution of bodies as shown in Figs. 2-4. The surface density of solid bodies is given by $\Sigma_s(a) = \int m n_s(m, a) dm = \int m^2 n_s(m, a) d \ln m$, so that we define the surface density of bodies in the logarithmic mass interval as

$$\Delta\Sigma_s(r, a) \equiv m^2 n_s(m, a), \quad (24)$$

with r corresponding to m . Fig. 2 shows $\Delta\Sigma_s(r, a)$. The collisional growth of bodies occurs inside-out. Orderly growth initially occurs so that $\Delta\Sigma_s$ have a maximum around radii of largest bodies in each annulus for $t \lesssim 1 \text{ Myr}$ (Fig. 2a,b). Larger bodies tend to have greater e and i for $r \gtrsim 10 \text{ m}$ (Fig. 3a,b and 4a,b). Density-fluctuation turbulent stirring and gas damping mainly control e and i for $r \gtrsim 10 \text{ m}$, while the fluid-dynamical turbulent stirring is dominant instead of that by density fluctuation for $r \lesssim 10 \text{ m}$. The runaway growth of bodies produces planetary embryos inside 8 AU by 4 Myr (Fig. 2c,d). The stirring by embryos increases e and i (Figs. 3c,d and 4c,d), which induces collisional fragmentation due to high speed collisions. Collisional fragments become smaller due to further collisions between themselves until radial drift, which reduces the surface density of bodies with $r \lesssim 10 - 100 \text{ m}$ (compare Figs. 2c and

2d). Planetary embryo formation in the outer disk induces collisional fragmentation and radial drift, which supplies small bodies in the inner disk. However, the net flux of small bodies reduces the surface density of bodies around planetary embryos in the inner disk. This stalls the growth of embryos (e.g., Kobayashi et al. 2010, 2011). In order to see detailed mass and orbit evolution, we focus on the evolution at 5.2 AU in the following paragraphs.

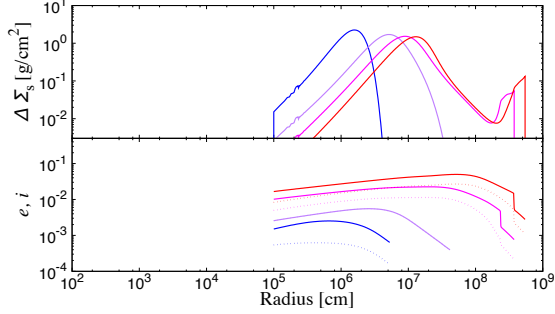


FIG. 5.— Size distribution of $\Delta \Sigma_s$ of bodies (top) and their eccentricities e (bottom; solid curves) and inclinations i (bottom; dotted curves) at 5.2 AU in a disk with $x_s = x_g = 3$ for $\alpha = 3 \times 10^{-3}$ without collisional fragmentation. The curves indicate those at 1.7×10^5 yr (blue), 8.7×10^5 yr (purple), 1.9×10^6 yr (magenta), and 3.2×10^6 yr (red). The time evolution results in the existence of large bodies, so that the curves move from left to right.

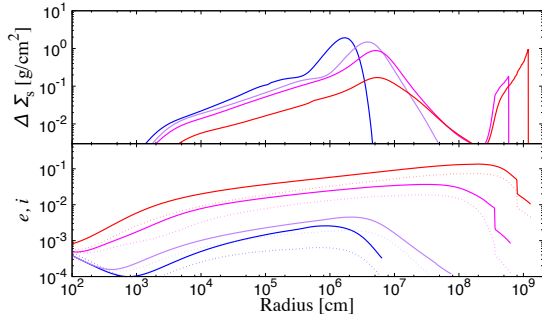


FIG. 6.— Same as Fig. 5 but with collisional fragmentation for primordial strength. The curves indicate those at 2.2×10^5 yr (blue), 7.2×10^5 yr (purple), 1.4×10^6 yr (magenta), and 3.3×10^6 yr (red).

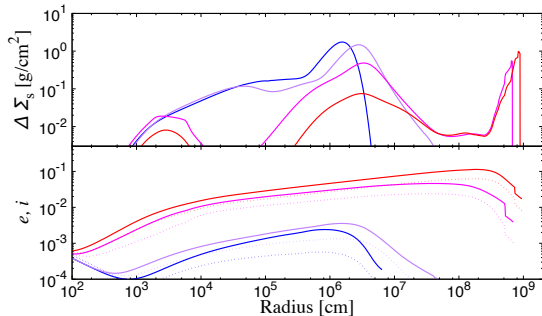


FIG. 7.— Same as Fig. 5 but with collisional fragmentation for monolith strength. The curves indicate those at 2.1×10^5 yr (blue), 4.9×10^5 yr (purple), 1.1×10^6 yr (magenta), and 3.1×10^6 yr (red).

4.2. Size and Velocity Distributions around 5 AU

As shown in Figs. 2–4, collisional fragmentation naturally occurs during planet formation and plays an important role for planet formation (e.g., Wetherill & Stewart 1993; Inaba et al. 2003; Kobayashi et al. 2010, 2011, 2012; Kobayashi & Dauphas 2013). Therefore collisional fragmentation is necessary to be taken into account for planet formation. For comparison, however, we first show the size and orbit evolution of bodies in the case without collisional fragmentation ($m_e = \Psi = 0$ in Eq. 6). Fig. 5 shows the evolution of $\Delta \Sigma_s$, e , and i of bodies at 5.2 AU in the 3MMSN disk with $\alpha = 3 \times 10^{-3}$, as a function of r corresponding to m . For $t \lesssim 1$ Myr, the surface densities $\Delta \Sigma_s(r)$ have single peaks, which move to large r . This is caused by orderly growth of bodies. The peak radius r_{pk} is approximated to be the mass-weighted average radius of bodies. For $t \gtrsim 1$ Myr, the size distribution becomes wider and then collisional evolution produces another peak at the high-mass end, which indicates planetary embryos. This is caused by the runaway growth of bodies. After the onset of runaway growth, r_{pk} does not change significantly so that the peak radius at the onset of runaway growth, r_{rg} , is approximated to be r_{pk} , which is estimated to ~ 100 km from the size distribution of bodies at ~ 1 Myr. The onset of runaway growth happens if $v_r \lesssim 1.5 v_{\text{esc}}$ for bodies of $r \sim r_{\text{pk}}$ (Kobayashi et al. 2016). Since $v_r/a\Omega \approx e$ and $v_{\text{esc}}/a\Omega \approx 6 \times 10^{-3}(r/100 \text{ km})$, we estimate $r_{\text{rg}} \approx 100$ km from the data of e at 1.9 Myr in Fig. 5, which is consistent with the mass distribution in Fig. 5.

The size distributions of bodies have single peaks at $r = r_{\text{pk}}$ prior to runaway growth, $t \lesssim 1$ Myr. Bodies with $r \lesssim r_{\text{pk}}$ have similar slopes of the size distributions of bodies. Even after runaway growth, bodies with $r \lesssim r_{\text{rg}}$ have similar slopes. The slope of the mass distribution of bodies is estimated by eye to $d \ln \Delta \Sigma_s(r)/d \ln r \approx 1.8$. For collisional cascade with Q_D^* and v_r independent of m , $d \ln n_s(m)/d \ln m = 1/2$ (Dohnanyi 1969; Tanaka et al. 1996). The slopes obtained from simulations without collisional fragmentation are steeper than that of the simple collisional cascade. On the other hand, the slopes of bodies with r ranging from $\approx r_{\text{rg}}$ to 10^5 km are $d \ln \Delta \Sigma_s(r)/d \ln r \approx -2.0$ in $t \gtrsim 1$ Myr. The collisional cross-section is proportional to $m^{5/3}/v_r^2$ due to gravitational focusing and $v_r \propto m^{-1/2}$ due to dynamical friction, which analytically gives $d \ln \Delta \Sigma_s(r)/d \ln r = -2$ (Makino et al. 1998). The slopes formed via runaway growth is roughly explained by gravitational focusing and dynamical friction. In more detailed analysis, the runaway-growth slopes bend slightly (see Morishima 2017).

Fig. 6 shows the evolution of bodies at 5.2 AU in the same condition as Figs. 2–4 (i.e., the case with collisional fragmentation for primordial strength). For $t \lesssim 1$ Myr, $\Delta \Sigma_s(r)$ have a single peak, although $\Delta \Sigma_s(r)$ have a long tail at low-mass side, which is produced by collisional fragmentation. These small bodies make collisional damping effective, which reduces v_r . Runaway growth occurs slightly earlier than the case without collisional fragmentation, resulting in $r_{\text{rg}} \approx 60$ km smaller than r_{rg} without fragmentation. After the onset of runaway growth ($t \gtrsim 1$ Myr), r_{pk} moves insignificantly. The stirring by planetary embryos created by runaway

growth increases e and i of surrounding planetesimals, which induces collisional fragmentation of planetesimals of $r \sim r_{\text{rg}}$. The solid surface density is decreased via collisional fragmentation and radial drift of resultant fragments (Kobayashi et al. 2010, 2011). Planetary embryos grow through the accretion of planetesimals and fragments until their depletion.

The size distributions of bodies have single peaks at $r = r_{\text{pk}}$ prior to runaway growth, which is similar to the case without collisional fragmentation. However, bodies smaller than the peaks have multiple slopes: The slopes are estimated by eye to $d \ln \Delta \Sigma_s(r)/d \ln r \approx 2.5$ for $r \ll 30$ m, $d \ln \Delta \Sigma_s(r)/d \ln r \approx 0.6$ from $r \approx 30$ m to $\sim 0.2r_{\text{pk}}$, and $d \ln \Delta \Sigma_s(r)/d \ln r \approx 2.0$ for $r \approx 0.2r_{\text{pk}} - r_{\text{pk}}$ (see Fig. 6). The slope for large bodies of $r = 0.2r_{\text{pk}} - r_{\text{pk}}$ is similar to that for no fragmentation, which is simply determined by collisional growth of bodies in orderly growth. The intermediate sized bodies for $r = 30$ m $- 0.2r_{\text{pk}}$, which are mainly produced by erosive collisions of bodies with $r \sim r_{\text{pk}}$, have so small e and i that collisional fragmentation is negligible. The collisional growth among them results in the slope determined by collisional cascade to the positive mass direction, $d \ln \Delta \Sigma_s(r)/d \ln r = 1/2$ (Tanaka et al. 1996). For bodies with $r \ll 30$ m, radial drift as well as the collisional cascade affects the mass distribution so that the slope is given by $d \ln \Delta \Sigma_s(r)/d \ln r = 5/2^1$. On the other hand, the runaway growth produces a different power-law size distribution of bodies with $r \gtrsim r_{\text{rg}}$; $d \ln \Delta \Sigma_s(r)/d \ln r = -2.0$, which is caused by runaway growth similar to the case without fragmentation. For $r \lesssim r_{\text{rg}}$, the slope is controlled by collisional fragmentation due to large e and i . Collisional cascade therefore occurs, resulting in $d \ln \Delta \Sigma_s(r)/d \ln r = (1 + 3p)/(2 + p)$ with $3p = d \ln Q_D^*/d \ln r - 2d \ln v_r/d \ln r$ (Kobayashi & Tanaka 2010). Although $d \ln Q_D^*/d \ln r$ depends on collisional velocities, $p \approx 0$ is roughly estimated and then $d \ln \Delta \Sigma_s(r)/d \ln r \approx 0.5$, which is similar to the slope for $r \sim 30$ m $- 50$ km. For $r \lesssim 30$ m, bodies have so small e and i that collisional fragmentation no longer occurs. The slope is determined by collisional growth and radial drift, which is almost the same as the slope of small bodies prior to runaway growth.

Fig. 7 shows the result of another simulation with monolith strength for the same disk condition. The evolution of size distribution is similar to the case for primordial strength; but the onset of runaway growth occurs slightly earlier, resulting in $r_{\text{rg}} \approx 30$ km. This is because the small bodies produced by collisional fragmentation prior to runaway growth results in slightly effective collisional damping. After the onset of runaway growth ($t \gtrsim 1$ Myr), forming planetary embryos induce collisional fragmentation of planetesimals, which mainly produces bodies with $r \sim 10$ m $- 10$ km through collisional cascade. The surface density $\Delta \Sigma_s(r)$ has a peak at the radius of 10–100 m. This is because the collisional cascade starting from collisional fragmentation of bodies with $r \sim r_{\text{rg}}$ is stalled by e and i damping by gas drag in the Stokes regime for bodies with $r \lesssim 10 - 100$ m

¹ Such bodies feel gas drag in the Stokes regime so that $v_r \propto r^{-2}$. The collisional cascade gives $(d \ln \Delta \Sigma_s(r)/d \ln r)_{\text{cas}} = 1/2$ and the modulation due to radial drift results in $d \ln \Delta \Sigma_s(r)/d \ln r = (d \ln \Delta \Sigma_s(r)/d \ln r)_{\text{cas}} - d \ln v_r/d \ln r$.

(Kobayashi et al. 2010). The magnitudes of such peaks depend on r_{rg} , Q_D^* , Σ_s , and so on. Planetary embryos mainly grow through collisions with bodies of $\sim r_{\text{rg}}$ or 10–100 m (Kobayashi et al. 2010, 2011). On the other hand, ~ 300 m-sized bodies are quickly destroyed via collisions with small bodies because of low Q_D^* .

The mass distribution prior to runaway growth is similar to the case with primordial strength. The slopes of small bodies are almost the same, while the population of small bodies is larger because of a high production caused by collisional fragmentation due to low Q_D^* . On the other hand, although runaway growth results in a slope for $r \gtrsim 30$ km $\approx r_{\text{rg}}$ similar to the case with primordial strength, bodies with $r \lesssim r_{\text{rg}}$ have a “wavy” structure, where the slopes $d \ln \Delta \Sigma_s(r)/d \ln r$ varies in small size ranges; $d \ln \Delta \Sigma_s(r)/d \ln r \approx 0.1$ for $r \approx 3 - 60$ km, $d \ln \Delta \Sigma_s(r)/d \ln r \approx 0.2$ for $r \approx 0.3 - 3$ km, $d \ln \Delta \Sigma_s(r)/d \ln r \approx -0.2$ for $r \approx 30 - 300$ m, and $d \ln \Delta \Sigma_s(r)/d \ln r \approx 0.2$ for $r \lesssim 30$ m ($t = 1.9$ Myr in Fig. 7). The slope controlled by collisional cascade is analytically estimated to $d \ln \Delta \Sigma_s(r)/d \ln r \approx 0.1$ for $r \gtrsim 500$ m and $d \ln \Delta \Sigma_s(r)/d \ln r \approx 0.0$ for $r \approx 30 - 500$ m. Collisional cascade may explain the slope only around $r \approx 3 - 60$ km. The “wavy” pattern for $r \lesssim 3$ km is formed due to large v_r^2/Q_D^* (e.g., Campo Bagatin et al. 1994; Durda & Dermott 1997; Thébault et al. 2003; Krivov 2007; Löhne et al. 2008). The value of v_r^2/Q_D^* becomes significant around $r = 500$ m because of minimum Q_D^* (see Fig. 1), which produces a bump at $r \approx 500$ m in the size distribution.

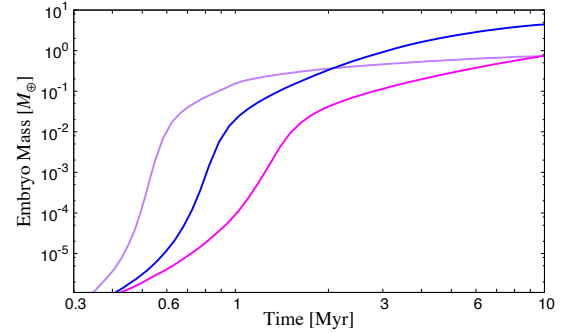


FIG. 8.— Time evolution of planetary-embryo masses for no fragmentation (magenta), monolith strength (purple), and primordial strength (blue).

Fig. 8 shows growth of planetary embryos obtained from simulations shown in Figs. 5–7. For $t \lesssim 0.4 - 1$ Myr, embryo masses M_E grow as $M_E \propto t^3$ because of orderly growth (Kobayashi et al. 2016). The onset of runaway growth occurs around 0.4–1 Myr, resulting in strong time dependence of M_E . The rapid growth occurs until $M_E \sim 10^{-2} - 10^{-1} M_\oplus$. The growth timescale in runaway growth depends on the collisional model, which is caused by different r_{rg} . After the rapid growth, slow growth occurs again, which is called oligarchic growth. Planetary embryos grow through surrounding planetesimals whose typical radii are r_{rg} (see Figs. 5–7). The viscous stirring by embryos increases e and i of planetesimals, which induces collisional cascade. Resultant bodies of $\sim 10 - 100$ m drift inward rapidly. Therefore, the oligarchic growth is stalled by the depletion of planetesimals due to collisional fragmentation and radial drift

of fragments. The growth of embryos at the oligarchic stage depends on Q_D^* for $r \lesssim r_{\text{rg}}$ that controls the depletion of the solid surface density (see Figs. 6 and 7). The oligarchic growth for primordial strength stalls later than that for melted materials. For primordial strength, the characteristic radii of planetesimals, r_{rg} , are large due to the late onset of runaway growth, which have great Q_D^* . The insignificant collisional depletion of planetesimals results in the long accretion of planetesimals onto embryos so that embryos grow to be massive. In addition, collisional cascade grinds planetesimals down to 10 – 100 m. Strong gas drag damps v_r for $r \lesssim 100$ m so that collisional cascade stalls without destructive collisions. The radius of bodies at the low mass end of collisional cascade, r_{cc} , depends on Q_D^* ; primordial strength has large r_{cc} . Bodies with $r \sim r_{\text{cc}}$ have so small v_r that they effectively accrete onto embryos, while their drift timescales are short because of strong gas drag. The accretion efficiency of bodies with $r \sim r_{\text{cc}}$ depends on r_{cc} (Kobayashi et al. 2010). For primordial material, embryos effectively grow via accretion of bodies with $r \sim r_{\text{cc}}$ because of slow radial drift for large r_{cc} due to great Q_D^* .

4.3. Turbulent Strength Dependence of Embryo Growth

We carry out the collisional-evolution simulations in 3MMSN disks with $\alpha = 3 \times 10^{-5} - 3 \times 10^{-3}$ for primordial Q_D^* , comparing with the results without collisional fragmentation (see Fig. 9). For weak turbulence ($\alpha \lesssim 10^{-4}$), the growth of embryos is similar to the case without fragmentation until embryos are larger than the Moon mass ($\sim 10^{-2} M_\oplus$). For $\alpha = 3 \times 10^{-3}$, the early collision fragmentation due to strong turbulent stirring leads to effective collisional damping, inducing the onset of runaway growth earlier comparing to the case without collisional fragmentation. After runaway growth, large embryos controls v_r instead of turbulence, which induces significant collisional fragmentation of planetesimals. Collisional cascade results in bodies of $r \sim r_{\text{cc}} \sim 10 - 100$ m. The effective accretion of such small bodies leads to the rapid growth of embryos (compare the results with or without collisional fragmentation). However, the growth is stalled by the depletion of small bodies due to collisional fragmentation and radial drift.

For small α the runaway growth occurs early, resulting in small r_{rg} . If we ignore collisional fragmentation, the early formation and growth of embryos due to small α results in large embryos (see Fig. 9). However, collisional fragmentation affects the growth of embryos. Small planetesimals tend to be destroyed via collision due to small Q_D^* for weak self-gravity (see Fig. 1). The stirring by small embryos increases v_r of planetesimals moderately, which can induce collisional fragmentation of planetesimals if small r_{rg} . Resultant fragments accelerate the growth of embryos initially, while the depletion of surrounding planetesimals stalls embryo growth. Weak turbulence (small α) results in small masses of embryos in the late stage ($t \gtrsim 4$ Myr in Fig. 9), while large α enhances r_{rg} and then M_E at the late stage.

Fig. 10 shows embryo growth for monolith Q_D^* . The α dependence is similar to the result for primordial Q_D^* ; higher α produces more massive embryos. However, final embryos are smaller. The accretion of small bodies with $r \sim r_{\text{cc}} \approx 10 - 100$ m contributes to embryo growth. However, the depletion of bodies with $r \sim r_{\text{cc}}$ due to

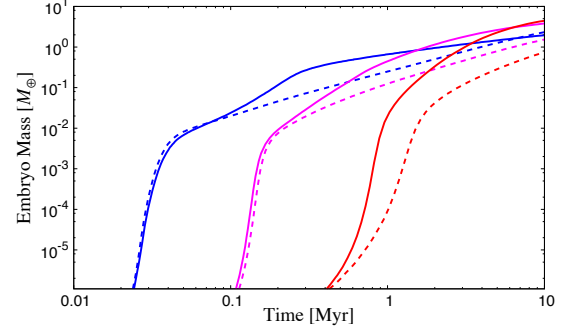


FIG. 9.— Time evolution of planetary-embryo masses in 3MMSN disk with $\alpha = 3 \times 10^{-5}$ (blue), 3×10^{-4} (magenta), and 3×10^{-3} (red) for collisional model with primordial Q_D^* (solid) and without fragmentation (dotted).

radial drift stalls embryo growth. Low Q_D^* for $r \sim 10 - 100$ m makes r_{cc} small. Therefore, the growth for monolith strength stalls earlier than that for the primordial strength (see Figs. 9 and 10).

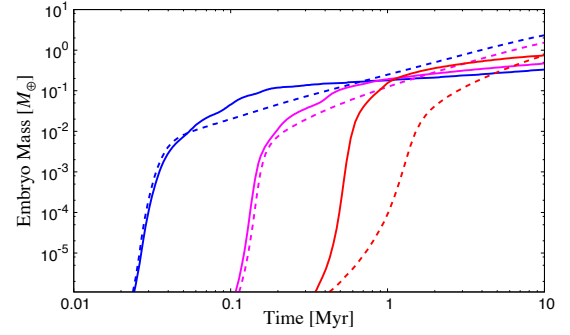


FIG. 10.— Same as Fig. 9, but for monolith Q_D^* (solid).

4.4. Forming Cores with Critical Core Masses

As discussed in § 2, gas giant formation via gas accretion requires embryos to be larger than $\sim 5 M_\oplus$ prior to significant gas depletion. Fig. 11 shows embryo masses M_E at 5.2 AU at 4 Myr with primordial strength. Massive embryos tend to be formed in the disks with strong turbulence (large α), while too strong turbulence cannot produce massive embryos because the onset of runaway growth is too late. In 3MMSN disks, embryos grow up to $1 - 2 M_\oplus$, which are too small to start gas accretion. However, the critical core mass depends on \dot{M}_E . To confirm the possibility of gas giant formation, we calculate the masses of static atmospheres around embryos, M_A , based on the analytical model for atmospheric radial density profile ignoring the gravity of atmospheres (Inaba & Ikoma 2003). The mass ratio M_A/M_E is smaller than 0.2 so that runaway gas accretion does not occur within 4 Myr. In the later stage, embryos grow more massive (see Fig. 9); $M_A/M_E \gtrsim 1/3$ at $t \approx 5$ Myr and 6–7 Myr for $\alpha = 3 \times 10^{-4}$ and 3×10^{-3} , respectively. In 2MMSN, the α dependence of M_E and M_A is similar to that in 3MMSN, while M_E and M_A are smaller. Therefore, embryos cannot reach the critical core mass within the disk lifetime $\lesssim 4$ Myr in the disks less massive than 3MMSN.

The collisional evolution of fluffy dust aggregates overcomes the radial drift barrier if the dust aggregates that

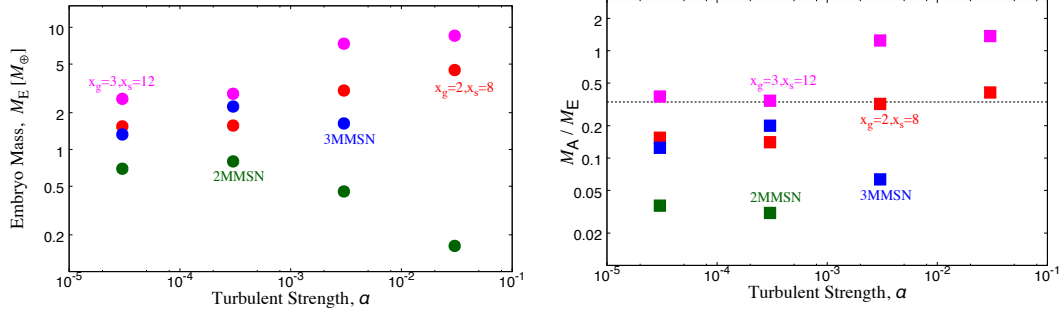


FIG. 11.— The masses of largest bodies, embryo mass M_E (left panel) and the mass ratio of atmosphere to core M_A/M_E (right panel) for the primordial strength bodies at 4 Myr at 5.2 AU in the disks with $x_g = x_s = 2$ (2MMSN; green), $x_g = x_s = 3$ (3MMSN; blue), $x_g = 2$ and $x_s = 8$ (red), and $x_g = 3$ and $x_s = 12$ (magenta). Once M_A/M_E exceeds $1/3$, runaway gas accretion to form gas giants occurs.

drift most effectively are controlled in the Stokes gas drag regime, resulting in planetesimals within ~ 10 AU (Okuzumi et al. 2012). During collisional evolution, the radial drift of dust aggregates induces a pile-up in the planetesimal forming region so that the solid surface density increases by a factor 3–4 (Okuzumi et al. 2012). According to the result, we set $x_s/x_g = 4$ ². In the solid-enhanced disks with $x_g = 3$ and $x_s = 12$, embryo masses at 4 Myr exceed $5M_\oplus$ for $\alpha \gtrsim 3 \times 10^{-4}$ so that their atmospheric masses M_A are much larger than $M_E/3$ (Fig. 11). For $x_g = 2$ and $x_s = 8$, M_E for $\alpha \lesssim 10^{-3}$ is similar to that in the case of 3MMSN, while large M_E for $\alpha \gtrsim 10^{-3}$ results in $M_A/M_E \gtrsim 1/3$. Fig. 12 shows the mass evolution of embryos in the disk with $x_g = 2$ and $x_s = 8$. The growth is stalled at $t \gtrsim 0.1$ Myr for $\alpha = 3 \times 10^{-4}$. The embryo growth occurs within ~ 1 Myr even for $\alpha \gtrsim 10^{-3}$, which forms massive cores. Therefore, in the solid-enhanced disks, runaway gas accretion for gas giant formation occurs within the disk lifetime ~ 4 Myr.

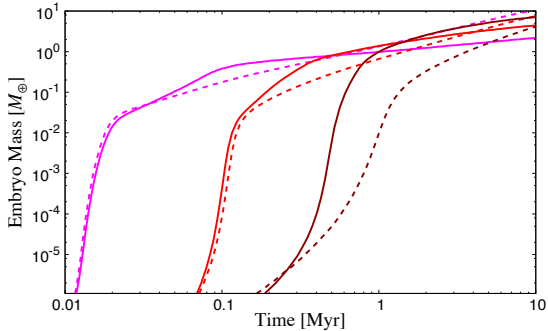


FIG. 12.— Same as Fig. 9, but in the disk with $x_g = 2$ and x_s for $\alpha = 3 \times 10^{-4}$ (magenta), 3×10^{-3} (red), and 3×10^{-2} (blown).

For monolith strength, embryo masses are smaller than that for primordial strength. In the 3MMSN disks, embryos are too small to start gas accretion. Even in the 5MMSN disk, M_A/M_E is smaller than 0.2. Therefore, gas giant formation via core accretion is difficult in the disk

² Although the solid enhancement due to the aggregate growth occurs within about 10 AU, the solid surface densities are set to be enhanced from 4.8 to 26 AU in the simulations. We also conduct the simulation with the outer disk edge at 9.4 AU for $\alpha = 3 \times 10^{-4}$ and 3×10^{-3} in the disks with $x_g = 3$ and $x_s = 12$ and then the masses of embryos at 4 Myr are the same within 20% for different outer edges. The supply from $\gtrsim 10$ AU is insignificant because the late formation of planetary embryos beyond 10 AU.

less massive than 5MMSN. In the solid enhanced disks with $x_g = 3$ and $x_s = 12$, embryo masses reach $\sim 1 - 2M_\oplus$ for $\alpha \gtrsim 3 \times 10^{-3}$. For $\alpha = 3 \times 10^{-2}$, $M_A/M_E > 1/3$. In the disk with $x_g = 5$ and $x_s = 20$, $M_A/M_E > 1/3$ for $\alpha \sim 3 \times 10^{-3}$. Therefore, melted bodies may form gas giant planets via core accretion in more massive disks, comparing to primordial material.

5. DISCUSSION

5.1. Growth Timescale

Prior to the runaway growth, the mass distribution of bodies is approximated to be a single mass population (Kobayashi et al. 2016), so that the collisional timescale at the onset of runaway growth is estimated to be

$$\tau_{\text{col}} \approx \frac{4i\rho_s r_{\text{rg}}}{3e\Sigma_s \Omega}. \quad (25)$$

The balance between turbulent stirring and gas drag gives i/e as ϵ prior to the onset of runaway growth (Kobayashi et al. 2016), while the gravitational interaction during runaway growth results in the energy equipartition, $i/e = 0.5$. The embryo formation timescale via runaway growth is proportional to τ_{col} with $i/e = 0.5$ (Ormel et al. 2010; Kobayashi & Tanaka 2010). The subsequent embryo growth timescale τ_g , which depends on the accretion of planetesimals or small bodies (Kobayashi et al. 2010, 2011), is simply approximated to be $\tau_g \approx 3\tau_{\text{col}}$;

$$\tau_g = 4.5 \left(\frac{x_s}{3}\right)^{-1} \left(\frac{r_{\text{rg}}}{30 \text{ km}}\right) \left(\frac{a}{5.2 \text{ AU}}\right)^3 \text{ Myr}. \quad (26)$$

The random velocity is determined by the balance between turbulent stirring and collisional damping prior to runaway growth. Once $v_r \approx 1.5v_{\text{esc}}$, runaway growth occurs. The radius of bodies at the onset of runaway growth is given by (Kobayashi et al. 2016)

$$r_{\text{rg}} = 32 \left(\frac{\alpha}{3 \times 10^{-3}}\right) \left(\frac{x_g}{3}\right)^2 \left(\frac{x_s}{3}\right)^{-1} \left(\frac{a}{5.2 \text{ AU}}\right)^{1.5} \text{ km} \quad (27)$$

From Eqs. (26) and (27), the timescale of embryo growth depending on turbulence strength is given by

$$\tau_g = 4.8 \left(\frac{x_g}{x_s}\right)^2 \left(\frac{\alpha}{3 \times 10^{-3}}\right) \left(\frac{a}{5.2 \text{ AU}}\right)^{4.5} \text{ Myr}. \quad (28)$$

As seen in Fig. 11, growing embryos at $t = 4$ Myr for $\alpha = 3 \times 10^{-3}$ are less massive than those for $\alpha = 3 \times 10^{-4}$ for $x_g = x_s$, while embryos at $t = 4$ Myr increases with

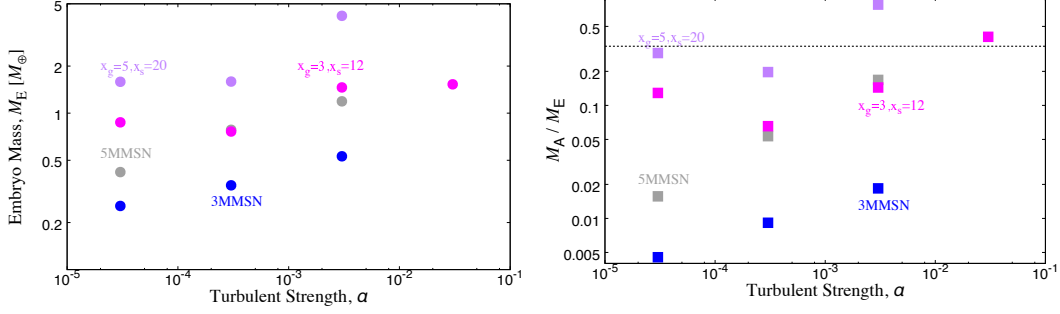


FIG. 13.— Same as Fig. 11, but for monolith strength in the disks with $x_g = x_s = 3$ (3MMSN; blue), $x_g = x_s = 5$ (5MMSN; grey), $x_g = 3$ and $x_s = 12$ (magenta), and $x_g = 5$ and $x_s = 20$ (purple),

α for $x_s/x_g = 4$. That is explained by the dependence of τ_g on x_s/x_g ; For $x_s/x_g = 4$, $\tau_g < 4$ Myr even for $\alpha \lesssim 3 \times 10^{-2}$, resulting in embryo formation within the disk lifetime.

Collisional fragmentation of planetesimals stalls embryo growth so that large r_{rg} tends to form embryos massive enough. The formation of cores with the critical core masses requires $r_{rg} \gtrsim 10$ km around 5 AU for primordial strength in the disks with $x_g \approx 3$. On the other hand, large r_{rg} results in a long embryo-growth timescale (see Eq. 26); $\tau_g \ll 4$ Myr is needed. These conditions are not satisfied for 3MMSN, while the solid-enhanced disks create massive cores for $\alpha \gtrsim 10^{-3}$ because of these conditions (see Fig. 12).

5.2. Planetary Migration and Gas Dispersal

Planetary embryos migrate due to density waves caused by interaction with disks; the migration timescale is estimated to be (e.g., Tanaka et al. 2002)

$$\begin{aligned} \tau_{\text{mig}} &= \gamma^{-1} \left(\frac{M_E}{M_*} \right)^{-1} \left(\frac{\Sigma_g a^2}{M_*} \right)^{-1} \left(\frac{c_s}{v_K} \right)^2 \Omega^{-1}, \\ &\approx 1.2 \gamma^{-1} \left(\frac{M_E}{M_\oplus} \right)^{-1} \left(\frac{\Sigma_g}{450 \text{ g cm}^{-2}} \right)^{-1} \left(\frac{c_s/v_K}{0.05} \right)^2 \\ &\quad \times \left(\frac{a}{5.2 \text{ AU}} \right)^{-1/2} \left(\frac{M_*}{M_\odot} \right)^{3/2} \text{ Myr}, \end{aligned} \quad (29)$$

where γ is the migration coefficient and the value of Σ_g is given from that of at 5.2 AU in the 3MMSN disk. In the isothermal disk, $\gamma \approx 4$ (Tanaka et al. 2002) and the co-rotation torque may reduce $\gamma \sim 1$ (Paardekooper et al. 2011). If the migration timescale is shorter than the time reaching the critical core mass, embryos are lost due to migration prior to gas giant formation. We here estimate the migration timescale for embryos obtained in our simulations using $\gamma = 1$.

For primordial strength, embryos as large as the critical core mass are formed within several Myrs in the disk with $x_s/x_g \approx 4$ for $\alpha \approx 10^{-3} - 10^{-1}$ (Fig. 11). Fig. 14 shows $3M_A/M_E$ at 5.2 AU for $\alpha = 3 \times 10^{-4}$ and 3×10^{-3} ; M_A becomes $M_E/3$ at $t \approx 2$ Myr and $3 - 4$ Myr for $\alpha = 3 \times 10^{-4}$ and 3×10^{-3} , respectively and embryos then reach the critical core masses. Using M_E obtained from the simulations and Eq. (29), we calculate τ_{mig}/t . Embryos may grow rather than migration unless $\tau_{\text{mig}}/t \lesssim 1$. Therefore, embryos migrate inward prior to the formation of embryos with the critical core masses; gas giant formation is inhibited by migration.

The disk dispersion timescale is required to be comparable to or shorter than τ_{mig} . For $\tau_{\text{gas}} = 1$ Myr, $\tau_{\text{mig}}/t > 1$ is satisfied in the simulations. However the gas surface density significantly decreases prior to the onset of the gas accretion of the core ($M_A = M_E/3$). Therefore, a more realistic gas dispersal should be taken into consideration.

For accretion disks with constant α for simplicity, the gas surface density is proportional to $\Sigma_g \propto (1 + t/\tau_{\text{dep}})^{-1.5}$ (Lynden-Bell & Pringle 1974), where $\tau_{\text{dep}} = \alpha^{-1} (v_K/c_s)^2 \Omega^{-1}/3$ at the disk radius r_{cut} of the exponential cutoff for the surface density. We estimate

$$\begin{aligned} \tau_{\text{dep}} &= 0.63 \left(\frac{\alpha}{3 \times 10^{-3}} \right)^{-1} \left(\frac{c_s}{0.1 v_K} \right)^{-2} \left(\frac{r_{\text{cut}}}{50 \text{ AU}} \right)^{3/2} \\ &\quad \times \left(\frac{M_*}{M_\odot} \right)^{-1/2} \text{ Myr}. \end{aligned} \quad (30)$$

Therefore, Σ_g may decrease on the timescale of 1 Myr.

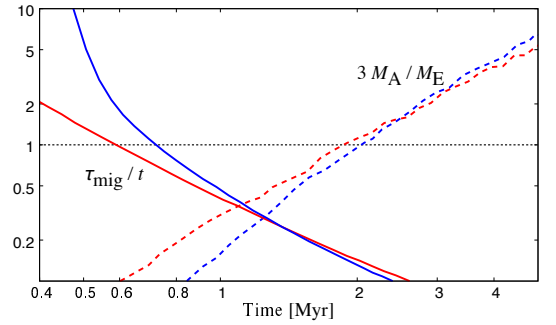


FIG. 14.— Dimensionless migration timescales τ_{mig}/t (solid curves) calculated from the results of simulations with primordial strength in disks with $x_g = 3$ and $x_s = 12$ for $\alpha = 3 \times 10^{-4}$ (blue) and 3×10^{-3} (red). Dotted curves indicate $3M_A/M_E$; The onset of runaway gas accretion is estimated from $3M_A/M_E = 1$.

We perform the simulations assuming $\Sigma_g \propto \Sigma_{g,0}/(1 + t/\tau_{\text{dep}})^{3/2}$ with $\tau_{\text{dep}} = 0.5$ Myr (Fig. 15), which mimics to the accretion disk. Embryos reach the critical core mass at $3 - 4$ Myr. The early gas depletion weakens the damping of eccentricity and inclination due to gas drag, and then the accretion of planetesimals on embryos is suppressed due to large e and i . However, small bodies produced by collisional fragmentation feel the Stokes gas drag, which is independent of gas density. The early gas depletion does not affect the accretion of such small bodies significantly. Therefore, embryos exceed the crit-

ical core mass within 4 Myr. On the other hand, the early gas depletion affects migration significantly. The gas depletion with $\tau_{\text{dep}} \lesssim 1$ Myr prolongs τ_{mig} , resulting in $\tau_{\text{mig}}/t > 1$. Therefore, embryos may start rapid gas accretion prior to migration.

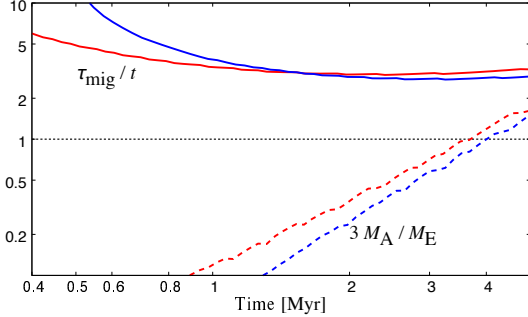


FIG. 15.— Same as Fig. 14, but for $\Sigma_g = \Sigma_{g,0}/(1 + t/\tau_{\text{dep}})^{3/2}$ with $\tau_{\text{dep}} = 10^6$ yr.

The disk with $x_g = 3$ initially has $\sim 17M_J$, where we set the disk edge at 50 AU and M_J is the mass of Jupiter. The disk mass decreases with $\propto (1 + t/\tau_{\text{dep}})^{-1/2}$ (Lynden-Bell & Pringle 1974) so that the disk mass becomes $6M_J$ at $t = 4$ Myr for $\tau_{\text{dep}} = 0.5$ Myr. The gas accretion of embryos with the critical core masses occurs not only from around embryos with the critical core masses but also from the whole disk during disk evolution (Tanigawa & Ikoma 2007), so that embryos may acquire an atmosphere comparable to Jupiter. Therefore, gas accretion occurs in such a depleting disk, which saves forming gas giants from type II migration (e.g., Ida & Lin 2008). It should be noted that τ_{dep} does not correspond to the disk lifetime inferred from the infrared observation. In the self-similar solution for accretion disks (Lynden-Bell & Pringle 1974), the disk evolution timescale prolongs for $t \gg \tau_{\text{dep}}$. Even for $\tau_{\text{dep}} \lesssim 1$ Myr, the large amount of gas remaining in several Myrs may be compatible with the disk lifetime from observations.

6. SUMMARY

We investigate planet formation in a turbulent disk. Turbulence suppresses the runaway growth of planetesimals. Once the random velocity of planetesimals is comparable to their escape velocity, runaway growth occurs (Kobayashi et al. 2016). The mass-weighted average radius during and after runaway growth is approximated to be that at the onset of runaway growth, r_{rg} . Embryos formed through runaway growth become massive through the accretion of planetesimals with $r \sim r_{\text{rg}}$. However, the stirring by massive embryos induces destructive collisions of planetesimals. Collisional cascade grinds bodies down to 10–100 m. Embryos grow through effective accretion of small bodies, while radial drift reduces small bodies. Eventually, the embryo growth stalls due to the depletion of bodies surrounding embryos via destructive collisions and radial drift. Therefore, the formation and growth of embryos strongly depends on the collisional properties for $r \sim r_{\text{rg}}$, which is controlled by

turbulent strength.

We have carried out simulations of collisional evolution of bodies with collisional strengths (Fig. 1) for the formation and growth of embryos in various disks, especially taking into account the stirring by density fluctuation caused by turbulence (Eq. 13). We find the followings.

- Strong turbulence delays the onset of runaway growth and increases r_{rg} . Embryos forming within disk lifetimes, $t \approx 4$ Myr, tend to be large for high α , while the onset of runaway growth is too late to form massive embryos within disk lifetimes for $\alpha \gtrsim 10^{-3}$. Cores massive enough are formed from $r_g \gtrsim 10$ km corresponding to $\alpha \gtrsim 10^{-3}$. However, the formation timescales of such cores are longer than the disk depletion time for $\alpha \gtrsim 10^{-3}$.
- Solid-enhanced disks are preferable for the formation of massive embryos. Such a local enhancement of solid can occur through radial drift of dust aggregates. For weak turbulence $\alpha \lesssim 10^{-3}$, embryo masses at $t = 4$ Myr are similar even in the enhancement of solid. However, embryos may grow within the disk lifetime even for strong turbulence $\alpha \gtrsim 10^{-3}$. Therefore, embryos are as large as the critical core mass within disk lifetimes in the gas disk more massive than 2MMSN.
- The embryo growth depends on collisional strength of bodies. We investigate collisional evolution for primordial and melted bodies using the model described in Eqs. (14)–(20) as shown in Fig. 1. For weak turbulence disks, embryo growth is independent of collisional strength until $M_E \approx 0.01M_\oplus$. However, once collisional fragmentation of bodies with $r \sim r_{\text{rg}}$ is effective, the embryo growth strongly depends on collisional strength. The low-mass end of collisional cascade is important for the efficiency of the accretion of bodies with $r = 10$ –100 m. The collisional strength $Q_D^* \gtrsim 10^7$ erg/g for $r \lesssim 1$ km, which is satisfied for primordial bodies rather than monolith material, is likely to form a massive core to be a gas giant (see Figs. 11 and 13).
- We have estimated the timescale of planetary migration during embryo growth. We have taken into account the gas density evolution similar to the accretion disk model. For example, embryos grow to the critical core mass for gas giant formation prior to migration in the disk initially containing 3MMSN gases for the dispersal timescale of 0.5 Myr (see Fig. 15). In spite of the short dispersal timescale, the disk mass at the onset of rapid gas accretion remains much larger than Jupiter masses. Therefore, moderately massive disks with short dispersal timescales are likely to form gas giants without significant migration.

The work is supported by Grants-in-Aid for Scientific Research (26287101, 17K05632, 17H01105, 17H01103) from MEXT of Japan and by JSPS Core-to-Core Program “International Network of Planetary Sciences”.

APPENDIX

PLANETARY ATMOSPHERE

The atmosphere structure is governed by (e.g., Inaba & Ikoma 2003)

$$\frac{dP}{dR} = -\frac{GM_E \rho_a}{R^2}, \quad (A1)$$

$$\frac{dT}{dR} = \begin{cases} -\frac{3}{4\pi\sigma_{SB}} \frac{\kappa L_e P}{T^4} & \text{if } \frac{3\kappa L_e P}{4\pi\sigma_{SB} T^4} < 1 - \frac{1}{\Gamma_2}, \\ -\left(1 - \frac{1}{\Gamma_2}\right) \frac{GM_E \rho_a}{R^2 T} & \text{otherwise,} \end{cases} \quad (A2)$$

where P is the pressure, T is the temperature, and Γ_2 is the second adiabatic exponent. In this study, we assume the atmospheric mass M_A is much smaller than M_E . However, if $M_A/M_E \gtrsim 1/3$, Eq. (A1) is invalid and then the rapid gas accretion forms gas giants (e.g. Mizuno 1980).

In Eq. (A2), the first term on the right hand side is given by the radiative energy transfer, while the second term is determined by convective transfer. Here, we derive a solution using the radiative term, although we take into account the both terms for simulations below § 3. Dividing Eq. (A2) by Eq. (A1) and integrating over P , we have

$$\rho_a = \frac{16\pi\sigma_{SB}GM_E T^3 \mu m_H}{3k\kappa L_e}. \quad (A3)$$

Inserting Eq. (A3) into Eq. (A2) and integrating it, we then obtain

$$T = \frac{GM_E \mu m_H}{4kR}. \quad (A4)$$

Substitution of Eq. (A4) into Eq. (A3) gives Eq. (1).

COLLISIONAL OUTCOME MODELING

Collisional outcome from the collision between bodies with m_1 and m_2 is expressed by m_e and $\Psi(m, m_1, m_2)$, which are determined as follows.

$$m_e = \frac{\phi}{1 + \phi}(m_1 + m_2), \quad (B1)$$

where ϕ is the dimensionless impact energy. Using the impact velocity v_{imp} and Q_D^* , which is the specific impact energy needed for ejection of half bodies, $\phi = m_1 m_2 v_{\text{imp}} / 2(m_1 + m_2)^2 Q_D^*$.

$$(m_1 + m_2)\Psi(m, m_1, m_2) = \begin{cases} m_e & (m > m_L), \\ m_e \left(\frac{m}{m_L}\right)^{2-b} & (m \leq m_L), \end{cases} \quad (B2)$$

where ϕ is the dimensionless impact energy and m_L is the largest mass of fragments produced by a single collision between bodies with m_1 and m_2 , given by

$$m_L = \frac{\epsilon_L}{1 + \phi} m_e = \frac{\epsilon_L \phi}{(1 + \phi)^2} (m_1 + m_2), \quad (B3)$$

b and ϵ_L are constants. We set $b = 5/3$ and $\epsilon_L = 0.2$. The timescale of collisional cascades is insensitive to values of b and ϵ_L (Kobayashi & Tanaka 2010).

REFERENCES

- Adachi, I., Hayashi, C., & Nakazawa, K. 1976, *Progress of Theoretical Physics*, 56, 1756
- Benz, W., & Asphaug, E. 1999, *Icarus*, 142, 5
- Campo Bagatin, A., Cellino, A., Davis, D. R., Farinella, P., & Paolicchi, P. 1994, *Planet. Space Sci.*, 42, 1079
- Dohnanyi, J. S. 1969, *J. Geophys. Res.*, 74, 2531
- Durda, D. D., & Dermott, S. F. 1997, *Icarus*, 130, 140
- Goldreich, P., & Ward, W. R. 1973, *ApJ*, 183, 1051
- Hayashi, C. 1981, *Progress of Theoretical Physics Supplement*, 70, 35
- Ida, S., & Lin, D. N. C. 2008, *ApJ*, 673, 487
- Ikoma, M., Nakazawa, K., & Emori, H. 2000, *ApJ*, 537, 1013
- Inaba, S., & Ikoma, M. 2003, *A&Ap*, 410, 711
- Inaba, S., Wetherill, G. W., & Ikoma, M. 2003, *Icarus*, 166, 46
- Inaba, S., Tanaka, H., Nakazawa, K., Wetherill, G. W., & Kokubo, E. 2001, *Icarus*, 149, 235
- Kobayashi, H. 2015, *Earth, Planets and Space* 67, 60
- Kobayashi, H., & Dauphas, N. 2013, *Icarus*, 225, 122
- Kobayashi, H., Ormel, C. W., & Ida, S. 2012, *ApJ*, 756, 70
- Kobayashi, H., & Tanaka, H. 2010, *Icarus*, 206, 735
- Kobayashi, H., Tanaka, H., Krivov, A. V., & Inaba, S. 2010, *Icarus*, 209, 836
- Kobayashi, H., Tanaka, H., & Krivov, A. V. 2011, *ApJ*, 738, 35
- Kobayashi, H., Tanaka, H., & Okuzumi, S. 2016, *ApJ*, 817, 105
- Krivov, A. V. 2007, *Dust in Planetary Systems*, 643, 123
- Löhne, T., Krivov, A. V., & Rodmann, J. 2008, *ApJ*, 673, 1123-1137
- Lynden-Bell, D., & Pringle, J. E. 1974, *MNRAS*, 168, 603
- Makino, J., Fukushige, T., Funato, Y., & Kokubo, E. 1998, *New A*, 3, 411
- Michikoshi, S., Kokubo, E., & Inutsuka, S.-i. 2012, *ApJ*, 746, 35
- Mizuno, H. 1980, *Progress of Theoretical Physics*, 64, 544
- Morishima, R. 2017, *Icarus*, 281, 459
- Ohtsuki, K. 1992, *Icarus*, 98, 20
- Ohtsuki, K., Stewart, G. R., & Ida, S. 2002, *Icarus*, 155, 436
- Okuzumi, S., & Ormel, C. W. 2013, *ApJ*, 771, 43

- Okuzumi, S., Tanaka, H., Kobayashi, H., & Wada, K. 2012 ApJ, 752, 106
- Ormel, C. W., Dullemond, C. P., & Spaans, M. 2010b, Icarus, 210, 507
- Ormel, C. W., & Klahr, H. H. 2010, A&A, 520, A43
- Ormel, C. W., & Okuzumi, S. 2013, ApJ, 771, 44
- Paardekooper, S.-J., Baruteau, C., & Kley, W. 2011, MNRAS, 410, 293
- Stevenson, D. J. 1982, Planet. Space Sci., 30, 755
- Stewart S. T., Leinhardt Z. M., 2009, ApJ, 691, L133
- Suyama, T., Wada, K., & Tanaka, H. 2008, ApJ, 684, 1310-1322
- Suyama, T., Wada, K., Tanaka, H., & Okuzumi, S. 2012, ApJ, 753, 115
- Takeuchi, T., & Ida, S. 2012, ApJ, 749, 89
- Tanaka, H., Inaba, S., & Nakazawa, K. 1996, Icarus, 123, 450
- Tanaka, H., Takeuchi, T., & Ward, W. R. 2002, ApJ, 565, 1257
- Tanigawa, T., & Ikoma, M. 2007, ApJ, 667, 557
- Thébault, P., Augereau, J. C., & Beust, H. 2003, A&A, 408, 775
- Völk, H. J., Jones, F. C., Morfill, G. E., & Röser, S. 1980, A&A, 85, 316
- Wada K., Tanaka H., Okuzumi S., Kobayashi H., Suyama T., Kimura H., Yamamoto T., 2013, A&A, 559, A62
- Wetherill, G. W., Stewart, G. R. 1989, Icarus 77, 330
- Wetherill, G. W., & Stewart, G. R. 1993, Icarus, 106, 190
- Youdin, A. N., & Goodman, J. 2005, ApJ, 620, 459